AIAA JOURNAL
Vol. 34, No. 8, August 1996

Computer-Controlled Multiparameter Flowfield Measurements Using Planar Laser-Induced Iodine Fluorescence

James M. Donohue* and James C. McDaniel Jr.†
University of Virginia, Charlottesville, Virginia 22903

A measurement technique for the mapping of complex compressible flowfields using planar laser-induced iodine fluorescence (PLIIF) is presented. Time-averaged values of all relevant flowfield properties are found: pressure, temperature, velocity, and, for mixing flowfields, injectant mole fraction. Several modifications have been made to a previous version of the PLIIF technique that allow multiple planes of data, needed for studying highly three-dimensional flowfields, to be collected and processed in greatly reduced time and with improved measurement accuracies. The technique is demonstrated with measurements in the flowfield of a Mach 2, rearward-facing step. Detailed comparisons are made to a computational fluid dynamics simulation of the flowfield. Differences between measured and simulated temperatures in the step recirculation region decreased from 21 to 4%, compared with previous broadband planar temperature measurements. Measurement accuracies are strong functions of the thermodynamic conditions. For the conditions seen in the step flowfield studied, estimated uncertainties range from 5–8% for temperature, 4–12% for pressure, 10–20 m/s for velocity, and 2–3% for injectant mole fraction. In regions very close to walls errors may be larger because of scattered laser light. The technique presented represents a unique tool that allows complex, compressible, three-dimensional flowfields to be mapped out completely and nonintrusively.

Nomenclature

A_{21} = Einstein spontaneous emission coefficient
B_{12} = Einstein spontaneous absorption coefficient
C_b = broadening cross section
C_I = impact shift constant
C_q = quenching cross section
f_1 = Boltzmann population fraction of lower level
I = laser intensity
N_{I_2} = iodine number density
P = pressure
P_{ratio} = pressure sensitive spectral parameter
Q = collisional quenching rate
T = temperature
T_{ratio} = temperature sensitive spectral parameter
u = velocity component in direction of laser sheet
V = Voigt function (convolution of Gaussian and Lorentzian functions)
v = frequency of the laser
v_0 = transition line center frequency
Δv_C = linewidth due to collisional broadening
Δv_D = linewidth due to Doppler broadening
Δv_I = impact shift
∞ = freestream values

I. Introduction

COMPRESSIBLE flowfields are of central importance to many modern aerospace applications, ranging from external aerodynamics and internal flows in propulsive devices to aeroacoustics and gasdynamic lasers. These practical flowfields tend to be very complex, exhibiting gasdynamic phenomena such as shock-wave/boundary-layer interactions, boundary-layer transition, flow separation and reattachment, and nonequilibrium and noncontinuum effects. Improved understanding of these complex compressible flow applications is being achieved through the combined efforts of modern computational fluid dynamics (CFD) and experimental techniques.

Laser-spectroscopic techniques are being increasingly utilized for measurements in compressible flows owing to their nonintrusive nature, their ability to measure specific parameters and specific flow species, and their capability for excellent spatial and temporal resolution.[1] Of these techniques, laser-induced fluorescence (LIF) is particularly attractive because of its relative simplicity, its inherent spatial resolution, and its strong signal, often permitting extension to planar imaging with planar laser-induced fluorescence (PLIF).

In nonreacting compressible flows, iodine has been used extensively as a seed fluorescing specie. Laser-induced iodine fluorescence (LIIF) techniques rely on seeding of iodine into the flowfield of interest and probing it with a laser, so that the resulting fluorescence can be used to extract information about the flow. Because molecular seeding is used, flow tracking issues are avoided. Very low levels of iodine (about 150 ppm) are needed so that thermodynamic properties of the flowfield air are affected negligibly. The iodine molecule is a particularly good candidate for LIF measurements because it has a large absorption cross section, fluoresces strongly in the visible and has a high vapor pressure, allowing for adequate seeding into room temperature air. Also, because it is a relatively heavy molecule, it contains numerous transition lines across a large range of frequencies, making it accessible to many different types of lasers. LIIF has evolved from qualitative flow visualization[2] to a technique for quantitative single-point measurement of multiple parameters,[3,4] to a planar (PLIIF) multiple-parameter measurement technique.[5,6] Tunable dye lasers have been used to make point-wise measurements of pressure, using the fluorescence intensity due to absorption line center excitation, and temperatures, using a two-line ratio technique.[7,8] To make planar measurements an argon laser was employed since this laser has adequate power for accurate planar imaging. Since only one strong iodine absorption line was accessible with this laser, temperature measurement was accomplished with broadband excitation of this single line.[9] The broadband argon laser has also been utilized for planar injectant mole fraction measurement with a ratio of two PLIIF images collected under different seeding conditions.[10] For planar pressure measurements, the argon laser was operated narrowband, by using an intracavity etalon, and manually tuned to measure the absorption line shape. Pressure is determined from the line broadening and a spectral model. Velocity is measured using the Doppler shift of the

Presented as Paper 93-0048 at the AIAA 31st Aerospace Sciences Meeting, Reno, NV, Jan. 11–14, 1993; received Feb. 7, 1995; revision received Nov. 20, 1995; accepted for publication Nov. 28, 1995.

*Research Associate, Department of Mechanical, Aerospace and Nuclear Engineering. Member AIAA.
†Professor, Department of Mechanical, Aerospace and Nuclear Engineering. Member AIAA.

absorption line with either broadband[11] or narrowband lasers.[12,13] At modest pressures (above about 15 kPa) the collisional impact shift must be accounted for in a Doppler-shift velocity measurement technique.[3,5,14]

The motivation for the work reported herein was to streamline the PLIIF measurement technique so that all flowfield parameters can be measured on multiple flowfield planes during a single operation of the wind tunnel. This objective forces the PLIIF technique to be altered in several ways. First, to avoid having to constantly reconfigure the laser, all parameters must be obtained with the laser operated narrowband. This means that the broadband temperature and mole fraction measurements need to be modified. Second, the experiment should be fully automated, using a computer to control the laser scan, position the laser sheet translation system, conduct the data acquisition, and control the camera imaging. Third, the computer system and data reduction algorithms must be upgraded to allow for on-line storage of the large image files and faster postprocessing of the data. With these improvements, it should be possible to obtain a complete flowfield mapping in a single experiment and have the data reduced the same day, instead of weeks later.

This paper describes the computer-controlled, multiple-parameter PLIIF flowfield mapping technique. The procedures used for extracting flowfield properties from the iodine fluorescence measurements are presented first. The experimental apparatus and system automation are discussed next. Finally, the technique is demonstrated with flowfield measurements obtained in a Mach 2 flow over a rearward-facing step. Application of the technique to the complete mapping of a more complex three-dimensional flowfield is presented in a separate paper.[15]

II. PLIIF Measurement Techniques

A. Iodine Fluorescence Modeling

To extract flowfield measurements from the fluorescence measurements requires an understanding of the iodine fluorescence process and how it is affected by the flowfield properties. Figure 1 shows a small region of the iodine absorption spectrum, at two different conditions, in the vicinity of the 514.5-nm argon ion laser to illustrate its thermodynamic dependence. The most striking difference between the two spectra shown in Fig. 1 is that the lines have broadened significantly in the higher pressure case because of collisional effects. Much of the structure of individual lines that was observable at lower pressure is lost due to the overlap of adjacent lines. Notice that the relative peak heights, which are functions mainly of temperature, have also changed.

Most of the development of iodine fluorescence modeling has been reported previously,[4,5,16,17] and so only a brief summary of the modeling used here will be given. The narrowband fluorescence signal S_f can be represented as

$$S_f = CI\left[\frac{A_{21}}{A_{21}+Q}\right] N_{I_2} \sum_i f_{1_i} B_{12_i} V(v - v_{0_i} - \Delta v_I, \Delta v_C, \Delta v_D) \tag{1}$$

where C includes fundamental constants and the optical collection efficiency. The term in square brackets is the ratio of the spontaneous emission rate to the total decay rate of the excited state (emission plus collisional quenching) and is known as the Stern–Volmer factor or fluorescence efficiency (predissociation and stimulated emission rates are neglected). The term N_{I_2} depends on the seeding fraction and the total number density. Because of line broadening, the absorption spectrum in this dense spectral region is significantly affected by relatively distant transitions. The model calculates the total fluorescence signal at each specific frequency by summing the individual contributions of the various transitions in the vicinity of the 514.5-nm argon laser line. For the work here, 133 transitions spanning a 200-GHz spectral region were used. The ground state Boltzmann population fraction f_1 depends on the ground state molecular quantum numbers and the local flowfield temperature. B_{12} includes the product of the Frank–Condon factor and the Holn–London factor, which are both functions of the molecular transition quantum numbers and are independent of the flowfield conditions. The transition quantum numbers, line center locations, and Frank–Condon factors are taken from Refs. 18 and 19. The Voigt function V describes the absorption line shape and is a function of the difference between the laser frequency and the impact-shifted transition line center $v - v_0 - \Delta v_I$, the collisional broadening, and the Doppler broadening.

Several of the terms in Eq. (1) are replaced with empirically derived functions of the thermodynamic conditions. The quenching rate Q scales with collisional frequency, so that the fluorescence efficiency can be rewritten as[16]

$$\left[\frac{A_{21}}{A_{21}+Q}\right] = \left[\frac{1}{1+Q/A_{21}}\right] = \left[\frac{1}{1+(C_q/A_{21})(P/T^{0.5})}\right] \tag{2}$$

where $C_q/A_{21} = 2.1\ \mathrm{K}^{0.5}/\mathrm{kPa}$. The collisional line width has been empirically determined to scale as[3]

$$\Delta v_C = C_b(P/T^{0.7}) \tag{3}$$

where $C_b = 4.2\ \mathrm{GHz\ K}^{0.7}/\mathrm{kPa}$. The hyperfine width of the transition (measured to be 0.8 GHz) contributes to the line shape at low pressures and is added to the Doppler line width. As well as generating line broadening, molecular collisions also produce a frequency shift of the absorption lines. This collisional impact shift was found to empirically scale with pressure and temperature as[3]

$$\Delta v_I = -C_I(P/T^{0.7}) \tag{4}$$

where $C_I = 0.39\ \mathrm{GHz\ K}^{0.7}/\mathrm{kPa}$. Note that the assumption is made that Q, C_b, and C_I are constant for all transitions.

The result of the modeling is that the narrowband fluorescence signal S_f can be represented as a complicated function of the pressure, temperature, velocity component in the beam direction u, and laser frequency v and is proportional to the laser intensity and to the number density of iodine present in the flow:

$$S_f = CIN_{I_2} f(P, T, u, v) \tag{5}$$

Terms such as C, I, and N_{I_2} appearing in Eq. (1) vary with spatial position and are difficult to correct for in data reduction procedures. This leads to systematic errors if absolute intensities are used to make measurements, as was done in previous LIIF techniques. In the present technique only ratios of signal levels, taken at the same spatial location but at different laser frequencies, are used to avoid these kinds of error.

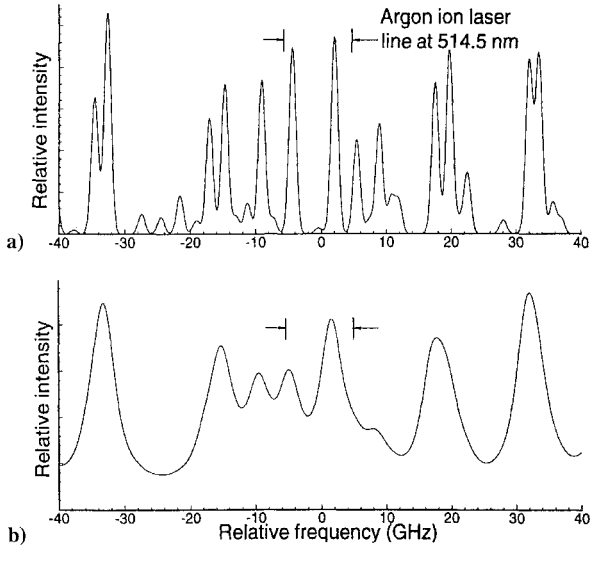

Fig. 1 Modeled iodine absorption spectrum, near the 514.5-nm argon laser line, at two different thermodynamic conditions: a) T = 300 k, P = 0.1 kPa and b) T = 167 k, P = 33 kPa.

B. Pressure and Temperature Measurement Technique

The new Spectra-Physics 2080 argon laser used for the work reported herein utilizes a strong magnetic field that causes Zeeman splitting of the 514.5 line, resulting in a gain profile wider than that

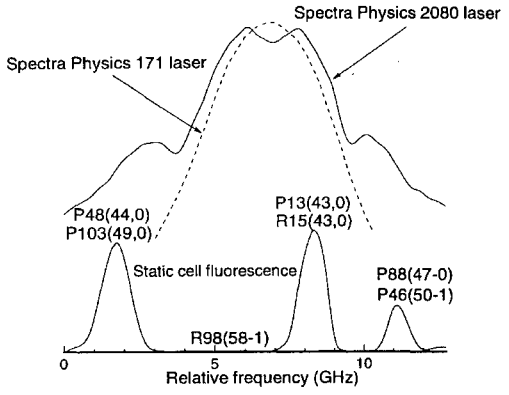

Fig. 2 Iodine transitions within the gain profiles of two argon lasers.

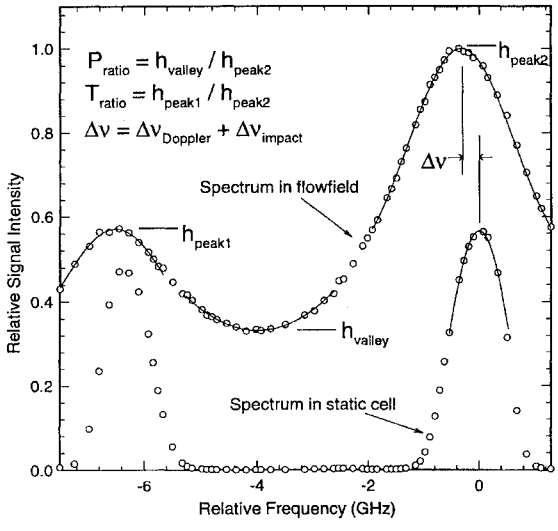

Fig. 3 Example measured fluorescence spectrum indicating curvefits through the left peak, valley, right peak, and static cell spectrum.

of argon lasers used previously. As shown in Fig. 2, a second strong iodine transition line falls within the gain profile of the new 2080 laser so that the more accurate two-line ratio temperature technique can now be used. Previous work with the Spectra-Physics 171 laser did not have access to this second line. The strong peak on the right is due to the blended P13, R15 rotational transitions from the 43-0 vibrational band. The peak on the left is due to a blending of the P48(44-0) transition with the P103(49-0) transition. Figure 3 shows a typical measured spectrum taken from a flowfield and a reference spectrum, taken simultaneously, in a low-pressure static cell. The peak and valley heights and the centerline locations are found by passing curves through the data in the local region of the peak or valley. For the peak locations a function consisting of a Gaussian plus a constant is used; for the valley, a second-order polynomial is used. The two ratio parameters, used to characterize the spectral shape, are defined in the figure. The left-to-right peak height ratio, or T_{ratio}, is sensitive to temperature because the different transitions have different ground state Boltzmann population fraction temperature dependencies. As the absorption lines broaden into each other with increased pressure, the relative height of the valley between the two peaks increases. The ratio of the valley height to the right peak height, or P_{ratio}, is chosen to be the pressure-sensitive parameter.

The shape of the fluorescence spectrum is a strongly coupled function of both thermodynamic variables. Because of this, the ratio parameters cannot, in general, be used to make accurate measurements individually. The coupled dependence can be accounted for with the use of correction factors, but this leads to complicated data reduction schemes. The coupled dependence was accounted for more directly in the previous planar pressure technique[5] by using the fully modeled fluorescence spectrum to generate a two parameter polynomial calibration function, but the data reduction was again complicated and required an iterative procedure. In the present technique the coupled thermodynamic dependence is accounted for in both the pressure and temperature measurements simultaneously. This is accomplished with a more straightforward graphical procedure described next.

The spectral parameters, P_{ratio} and T_{ratio}, are functions of both pressure and temperature; however, for each (P_{ratio}, T_{ratio}) pair there corresponds a unique (P, T) pair. The fluorescence model is used to calculate P_{ratio} and T_{ratio} for a matrix of pressures and temperatures. The results are shown as the grid at the top of Fig. 4. The grid can be thought of as a mapping definition to change from the (P, T) coordinate system to the (P_{ratio}, T_{ratio}) system. The mapping definition is then inverted so that P and T can be found from measured values of P_{ratio} and T_{ratio}. This mapping approach can be used for any set of parameters chosen, as long as the mapping definition is unique. If the mapping grid used is fine enough, linear interpolation can be used to quickly and accurately determine the pressure and temperature from the two measured parameters. The mapping plane also clearly illustrates variations in the sensitivity of the technique at different conditions by the changing density of grid lines in the inverted grid. Where grid lines are packed closely together, relatively small errors in the measured parameters lead to relatively large errors in the measured pressure or temperature. It is clear that the best measurement accuracy is to be expected at low pressures. Also it is apparent that at high temperatures and low pressure, where the grid lines move parallel to the T_{ratio}, P_{ratio} axes, the measurement parameters are more decoupled. Notice that at high pressure and low temperature the grid mapping plane contains no points. This is

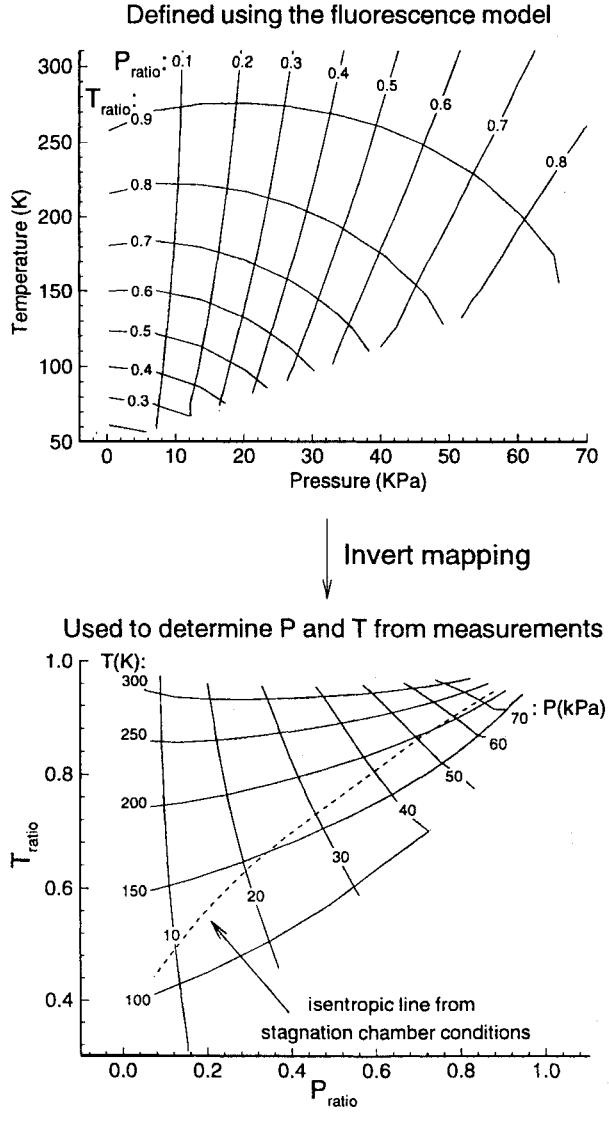

Fig. 4 Coordinate transformation between the (P, T) and (P_{ratio}, T_{ratio}) planes.

because in this region the spectrum has broadened so much that it no longer has a double peak shape and the measurement procedure breaks down. In the tests presented, however, this region is located below the isentropic line defined by the inlet air stagnation conditions, and so it is unlikely that conditions in this region will ever be encountered in the flowfield.

C. Velocity and Injectant Mole Fraction Measurement Techniques

The techniques for measuring velocity[3,5,14] and injectant mole fraction[10] have been well documented previously, and so only a brief description will be given. The velocity is determined by measuring the frequency shift of the measured spectrum in the flowfield relative to an unshifted spectrum measured in a low-pressure static cell. The measurement is indicated in Fig. 3 as Δv. The shift is due to the Doppler effect, because flowfield molecules have a velocity component in the direction of the laser sheet, and due to collisional effects, known as the impact shift. The impact shift can be accounted for using a counterpropagating beams approach[20,21] or calculated from the previously determined pressure and temperature measurement.[3,5] The Doppler shift gives the velocity component in the direction of the laser sheet. Two directions are needed two determine the two velocity components in the plane.

For the measurement of injectant mole fraction, an image is taken with iodine seeded only in the injector. The iodine is used to tag the injectant air. To account for the thermodynamic dependence of the signal levels, this image is divided by a second image where the tunnel is run with iodine seeded everywhere in the flowfield.[10] Equation (1) can be used to show that the signal ratio gives the ratio of number densities in the two seeding conditions, which is proportional to the injectant mole fraction. The ratio is not equal to the injectant mole fraction because the seeding level for the each seeding condition may be different. The proportionality constant can be determined by using the measured value in the injector core, where the injectant mole fraction is unity. The measurement can be made with the laser operated broadband, as was done previously, or with the narrowband laser. A slight increase in measurement uncertainty is expected since less power is available in narrowband mode.

III. Experimental Apparatus and Procedures

A. Experimental Setup

Experiments are carried out in a continuous-flow Mach 2 wind-tunnel facility specifically designed for iodine compatibility. A two-dimensional Laval nozzle exits into a test section configured with a rearward-facing step geometry. The test section has a 21.3-mm height, a 30.5-mm width, and a 3.18-mm step height. The pressurized supply air is filtered and dried before it enters the wind tunnel. The stagnation pressure and temperature are monitored throughout the testing period by the computer data acquisition system. The facility is equipped to seed iodine into the freestream air, into the injector air (if mixing studies are to be performed), or into both simultaneously. To allow optical access to the flowfield, three of the test section walls are made of fused silica.

Figure 5 illustrates the optical arrangement for the PLIIF imaging. A 200-μ-thick laser sheet is created from the Spectra-Physics 2080 argon ion laser beam using a cylindrical lens to spread the beam and a spherical lens to collimate the beam and focus it at the center of the wind-tunnel test section. A liquid-nitrogen-cooled charge-coupled device (CCD) camera is used to image the resulting iodine fluorescence. The Photometrics CH210 camera used was chosen because of its high degree of linearity, its low dark current noise levels, and the high resolution it provides (516 × 516 pixels with 14-bit intensity levels). To position the laser sheet at the desired location, the optics are mounted on a computer-controlled translation stage. All lenses and mirrors and the camera are mounted on the same translation stage so that the alignment of the camera and the laser sheet is maintained as the sheet is scanned throughout the flowfield.

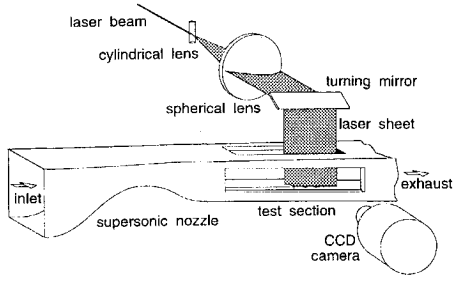

Fig. 5 Optical setup for planar flowfield imaging.

The laser is operated in narrowband mode by using an intracavity etalon to choose the frequency given by a single axial mode of the laser cavity. By increasing the optical thickness of the etalon, successive axial modes can be chosen and the laser can be tuned across the gain profile. A portion of the laser beam is split off and used to monitor the laser's power and frequency. The fluorescence from a low-pressure iodine static cell is monitored with a photomultiplier tube and used as an absolute frequency reference. The beam of a second argon ion laser, operated at constant power and in broadband mode, is directed inside the flowfield and to the edge of the camera's field of view. The fluorescence from this laser beam is used to monitor variations in the iodine seeding level during an experiment.

B. Data Acquisition and System Automation

Because the quantity of data collected is very large and the post-processing required is extensive for these types of planar measurements, sufficient computational facilities and a reasonable level of system automation are required. For 20 spatial flowfield locations and 2 velocity components in each plane, approximately 2400 images must be acquired if 60 discrete laser frequencies are used to generate the spectra. This corresponds to about one gigabyte of raw data to be stored and processed. To handle this large amount of data, the computer system had to be upgraded and now consists of three computers: a 486-based PC used for the main data acquisition and control, a 386-based PC used to control the camera operation, and an IBM RS6000 workstation attached using a fast data transfer ethernet connection to store and process the data.

Figure 6 shows a schematic of the data acquisition and control setup. The 486 personal computer acquires stagnation conditions, static cell fluorescence levels, and laser power meter readings using a data acquisition board with A/D inputs. Communication to the translation stage positioning system and to the CCD camera controller system is done over a General Purpose Interface Bus (GPIB). An analog output from the 486 PC is sent to the camera controller to trigger an exposure. The 386 PC controls transfer of data from the camera and sends the image data directly to the workstation by defining a directory location on the workstation as a virtual disk. Data reduction is performed on the workstation and decreases image

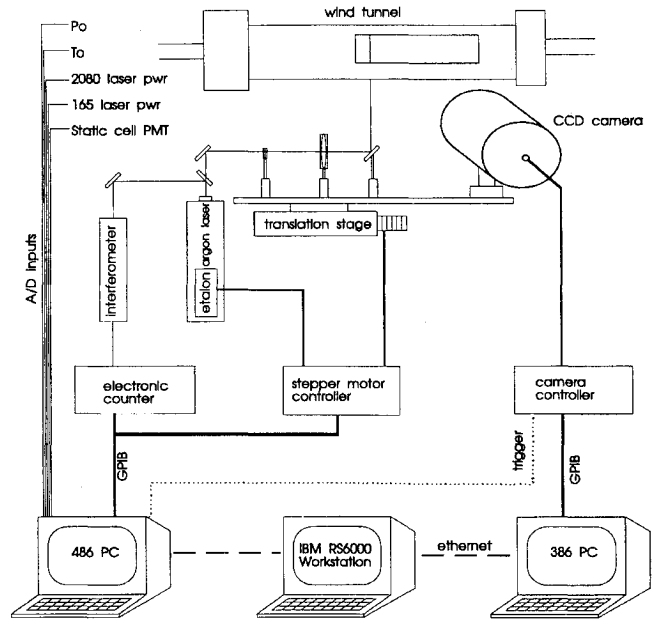

Fig. 6 Diagram of data acquisition and control system for automating the PLIIF measurements.

processing time by a factor of about 50 compared with the processing time required previously on the 386 personal computer.

Except for the laser tuning, data acquisition and control is accomplished through standard procedures as described earlier; however, no easily automated system was available for monitoring and control of the laser frequency. The laser frequency was monitored, when manual tuning was performed, by looking for laser mode hops on an oscilloscope trace of the scanning interferometer. By counting mode hops as the etalon is tilted, and using the known axial mode spacing for the laser cavity, a reliable frequency reading could be made. To automate this process an electronic counter is used to measure the time interval between the beginning of the interferometer trace and the spike at the laser frequency location. By calibrating the time scale into frequency units, the integral number of mode hops that occur during the scanning of the laser can be determined. Several types of remotely controlled etalons were investigated. A temperature-tuned etalon was found to respond too slowly because of its thermal inertia. A piezo-electrically tuned etalon system produced poor laser power levels, was difficult to align, and exhibited thermal drift. A tilting solid glass etalon, with a temperature stabilization oven, gave the best power and stability characteristics and was used for the final test setup. Tuning was accomplished by turning the etalon's tilting adjustment screw with a remotely controlled stepper motor. A constant output power level of 1.5 W was possible over the entire tuning range.

C. Image Collection and Data Reduction Procedures

The data collection process consists of nested loops over laser frequency and sheet location. The frequency loop is chosen as the inner loop to avoid errors associated with laser frequency drift over long periods, since acquisition times for multiple measurement planes can be several hours. For the duration of the image exposure, tunnel stagnation pressure, and temperature, laser powers and static cell fluorescence readings are collected. The 386 personal computer sends the image collected to the workstation over the ethernet line and then arms the camera for a new exposure. Simultaneously the 486 personal computer moves the laser to a new frequency location while monitoring the counter for mode hops. A new exposure is then triggered by the 486 and the process repeated across a range of about 10 GHz and 60 images. When the frequency scan is completed, the two additional images needed for the injectant mole fraction measurement and a background measurement are acquired. The sheet is repositioned after measurements at each location are finished until the desired spatial mapping is completed.

The image intensities are corrected for image-to-image laser power variations. A background image, also corrected for laser power variations, is then subtracted. To allow for seeding fraction variations, the signal is then divided by a corrected fluorescence intensity at the location of the seeding fraction beam. A measured iodine absorption spectrum is constructed at each individual pixel location, and curvefits are passed through the data points so that experimental values of the T_{ratio} and P_{ratio} and Δv can be found (see Fig. 3). The mapping method previously discussed can now be used to find the pressure and temperature, and the velocity found after correction for the impact shift. A measurement in the same plane but with a different sheet direction is used to determine the two components of velocity in the measurement plane.

D. Uncertainty Analysis

The uncertainty in the measurements are primarily caused by two sources of random error, inaccuracies in the fluorescence measurements and unsteadiness of the inlet stagnation conditions, and one source of systematic error, inaccuracies in the fluorescence modeling. Because the fluorescence signal levels and the sensitivity in the transformation from (T_{ratio}, P_{ratio}) to (P, T) vary strongly with the thermodynamic conditions, the measurement uncertainties also depend strongly on the thermodynamic conditions. In this section, estimates of this dependence are made for the pressure, temperature, and velocity measurements. The uncertainty in the injectant mole fraction measurements have been estimated to be about 2–3%.[6]

The uncertainty in the individual data points that make up the measurement of the fluorescence spectrum (see Fig. 3) is about 3% and is caused by photon shot noise and inaccuracy in the laser power measurement. By using the least-square curvefitting procedure described, the uncertainty in the measured T_{ratio} and P_{ratio} parameters is about 1%. The fluorescence model is estimated to have a worst case uncertainty of 0.02 for T_{ratio} and 0.015 for P_{ratio}. The two effects can be combined to give the uncertainty in the ratio parameters:

$$\Delta P_{\text{ratio}} = \sqrt{(0.01 P_{\text{ratio}})^2 + (0.015)^2} \tag{6}$$

$$\Delta T_{\text{ratio}} = \sqrt{(0.01 T_{\text{ratio}})^2 + (0.02)^2} \tag{7}$$

The overall uncertainty in P and T can now be found by combining the effects of uncertainty in the ratio parameters and a 0.5% uncertainty due to variations in the stagnation conditions:

$$\Delta P = \sqrt{\left(\frac{\partial P}{\partial P_{\text{ratio}}}\Delta P_{\text{ratio}}\right)^2 + \left(\frac{\partial P}{\partial T_{\text{ratio}}}\Delta T_{\text{ratio}}\right)^2 + (0.005P)^2} \tag{8}$$

$$\Delta T = \sqrt{\left(\frac{\partial T}{\partial P_{\text{ratio}}}\Delta P_{\text{ratio}}\right)^2 + \left(\frac{\partial T}{\partial T_{\text{ratio}}}\Delta T_{\text{ratio}}\right)^2 + (0.005T)^2} \tag{9}$$

The partial derivatives in the preceding expressions represent the sensitivities in the (T_{ratio}, P_{ratio}) to (P, T) transformation and are given by the gradients in the mapping plane in Fig. 4. The upper two plots in Fig. 7 show the resulting uncertainties in P and T. For conditions typical of the step flowfield presented in the next section, uncertainties range from about 4–12% for pressure and 5–8%

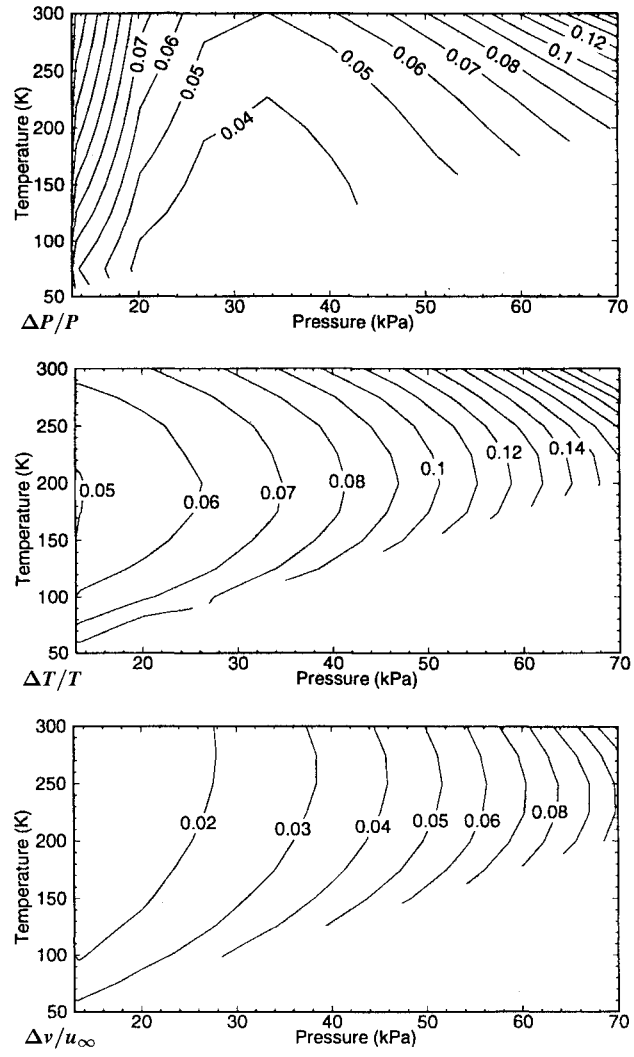

Fig. 7 Calculated experimental uncertainties as a function of pressure and temperature (velocity values are nondimensionalized with the freestream of the rearward-facing step flowfield, u_∞ = 520 m/s).

for temperature. The uncertainty in the fluorescence modeling contributes about twice as much to the overall uncertainty in P and T when compared with the contribution from the fluorescence measurement inaccuracies. The contribution from stagnation condition variations is considerably smaller. This indicates that better calibration of the model could significantly improve accuracies.

The uncertainty in the velocity measurement is caused by uncertainty in measuring the line center location and uncertainty in the impact shift correction. Uncertainty in measuring the relative line center locations, Δv_{cl}, is about 0.007 GHz but varies considerably with signal levels. The uncertainty in the impact shift relation [Eq. (4)], is caused by uncertainty in the impact shift constant and uncertainty in the pressure and temperature values just determined. The overall uncertainty in the impact shift relation is found by taking partial derivatives with respect to each term in Eq. (4) and combining the errors:

$$\Delta v_I = \sqrt{\left(P/T^{0.7}\Delta C_I\right)^2 + \left(C_I/T^{0.7}\Delta P\right)^2 + \left(C_I P/T^{1.7}\Delta T\right)^2} \tag{10}$$

Uncertainty in the impact shift constant is taken to be 0.02 GHz/K$^{0.7}$/kPa. The total uncertainty in velocity, caused by the Doppler shift of the spectrum in the direction of the laser beam, is then found by combining the uncertainty in the measured shift with the uncertainty in the impact shift and multiplying by the wavelength of the laser ($\lambda = 514.5$ nm):

$$\Delta\text{velocity} = \lambda\sqrt{(\Delta v_{cl})^2 + (\Delta v_I)^2} \tag{11}$$

The resulting uncertainty estimate for velocity measurement in the direction of the laser sheet as a function of the pressure and temperature is shown in the bottom plot in Fig. 7. The velocity uncertainty is nondimensionalized with the freestream velocity of the rearward-facing step flowfield, which is about 520 m/s. The values range from about 2–4% or 10–20 m/s for the conditions seen in the flowfield. The contribution to the overall velocity uncertainty from the uncertainty in the impact shift dominates the contribution from the measurement of the line center location.

There are several advantages, with regard to uncertainty, in this revised version of the PLIIF technique over the previous version: 1) use of only ratio parameters eliminates several sources of systematic error present in the previous version where absolute intensities were used; 2) pressure and temperature can now be determined directly, whereas in the previous PLIIF technique a point in the flowfield with known conditions was required; and 3) in the previous PLIIF technique, pressures were measured most accurately at low pressure but temperatures could only be measured accurately at pressures above 20 kPa. In the present technique, pressure and temperature measurements are most accurate at the same range of pressure; 4) improved accuracy in the pressure and temperature measurement leads to a more accurate impact shift calculation and, therefore, a more accurate velocity measurement.

IV. Measurements in a Rearward-Facing Step Flowfield

The PLIIF techniques were applied to a Mach 2 rearward-facing step flowfield to demonstrate the experimental technique in a flowfield that is reasonably well understood.[22] The supersonic flow behind a rearward-facing step is an excellent test case because it is two dimensional yet contains many of the complexities of compressible flowfields of interest. Important flow features, such as expansion fans, shock waves, and a separated recirculation region, are present. A comparison of pressure and temperature distributions predicted by a SPARK CFD code simulation[23] and the experimental PLIIF results are shown in Figs. 8 and 9. The inflow has a Mach number of 2.0 with stagnation conditions of 300 K and 260 kPa. The coordinates are nondimensionalized by the step height, and the values of temperature and pressure are nondimensionalized using the freestream conditions, 167 K and 33.3 kPa.

The expansion fan is seen most clearly in the pressure plots, where pressure decreases to about 0.45 in the experiments and to 0.35 in the calculations. This 22% difference appears to be caused by a different amount of flow turning in the experiment and simulation. As seen in the temperature distributions, there is a difference in the angle of the recirculation shear layer in the numerical and experimental results. A thicker shear layer will tend to turn the main flow less, which appears to be occurring in the experiments relative to the calculation. Since the thickness of the incoming boundary layers are in good agreement, the discrepancy in the shear layer thickness is most likely caused by turbulence modeling inaccuracies. Precise numerical prediction of separation zones are generally difficult because of their turbulent, unsteady nature. The measured nondimensional temperature of 1.7 in the recirculation region is in good agreement with the calculated value. Previous pointwise LIIF temperature measurements indicated a value of 1.6 in this region; however, wall measurements using a thermographic phosphor technique indicated a value of 1.71.[22] The location of the reattachment shock, which is captured accurately in the experimental images, is only slightly further downstream in the calculation. Close to walls,

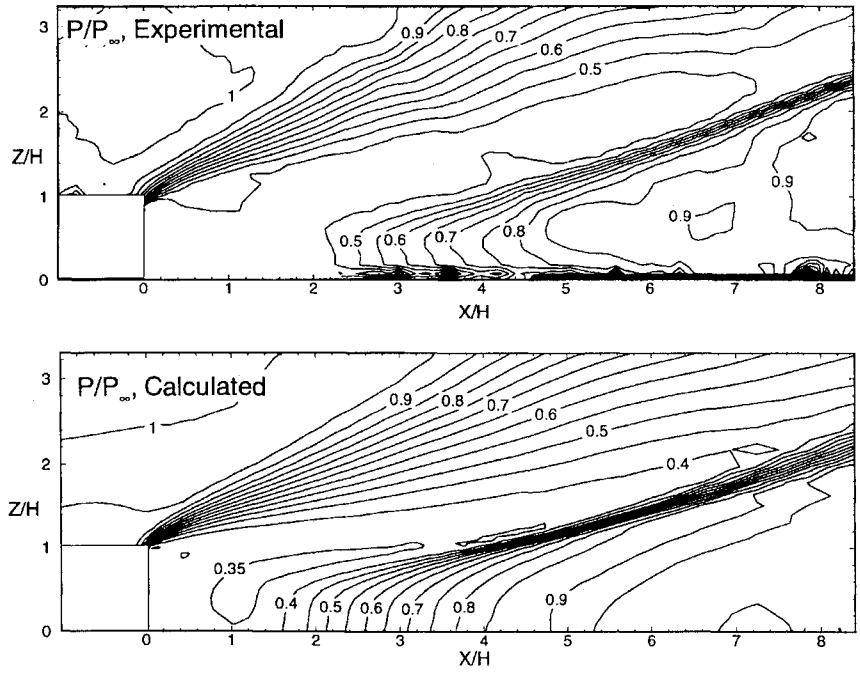

Fig. 8 Pressure distribution in the rearward-facing step flowfield (nondimensionalized by the freestream static pressure).

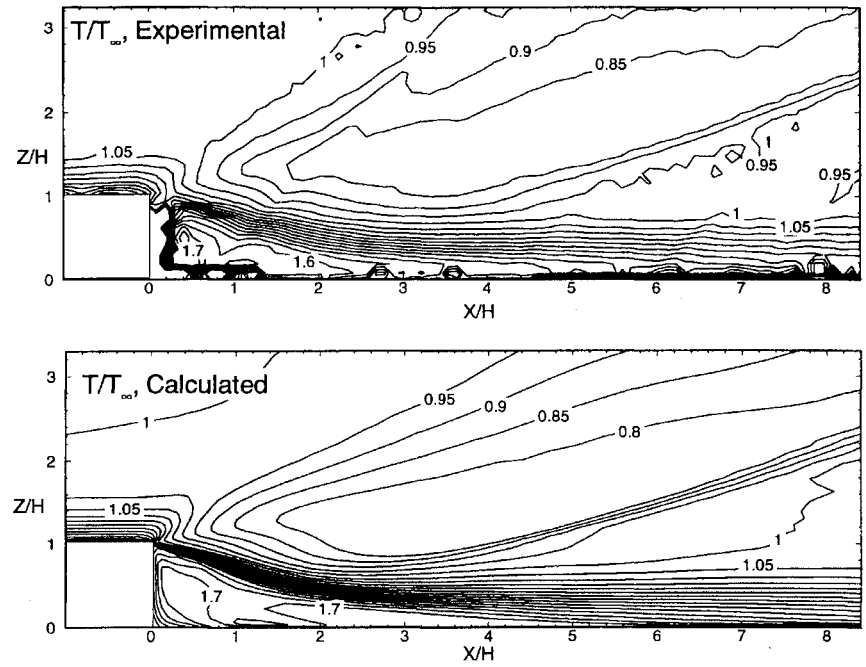

Fig. 9 Temperature distribution in the rearward-facing step flowfield (nondimensionalized by the freestream static temperature).

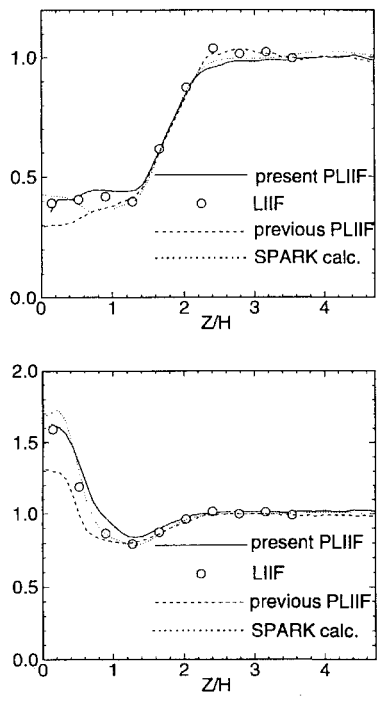

Fig. 10 Pressure and temperature results from the present PLIIF technique, the previous pointwise LIIF technique, the previous PLIIF technique and the SPARK calculation taken along a line of constant X/H in the rearward-facing step flowfield: P/P_∞ at $X/H = 1.75$ and T/T_∞ at $X/H = 1.75$.

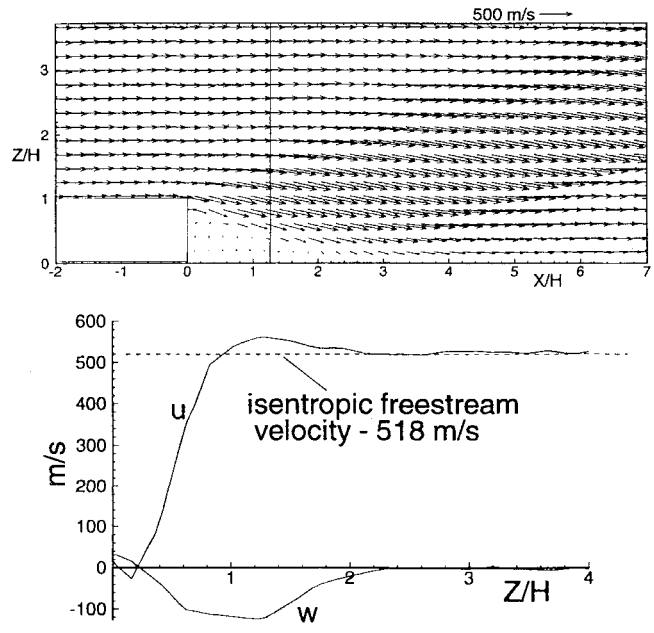

Fig. 11 Velocity measurements in the rearward-facing step flowfield: u and w profiles at $X/H = 1.25$.

because of high levels of scattered light, measurements errors are high. In particular, just behind the step, the camera has a direct view of the laser sheet striking the wall causing the unreasonable contour levels seen in the temperature results in Fig. 9.

Results along a profile at $X/H = 1.75$ are extracted from the PLIIF and SPARK calculation results and presented in Fig. 10. Also included are the measurements made with the pointwise LIIF and the previous PLIIF techniques presented in Ref. 22. The present PLIIF temperature measurements show considerably closer agreement to the LIIF measurements and the calculation in the warm region near the wall than the previous PLIIF technique. The difference in the amount of flow turning, as discussed earlier, contributes to differences in the minimum pressure seen in the calculated and measured results.

To demonstrate the velocity technique, Fig. 11 shows planar velocity measurements in the rearward-facing step flowfield. The velocity technique is essentially the same as was used previously, except that the impact shift constant used here[24] is about 25% higher than that in Ref. 6. Results along a profile taken through the planar data at $X/H = 1.25$ are also shown. The velocity field looks as expected, with vectors parallel to the walls at the inlet and after the reattachment shock. The horizontal component of velocity in the freestream agrees with the isentropic Mach 2 value. The zero freestream vertical component is also as expected.

The agreement shown here between results using the present PLIIF technique and results from previous iodine fluorescence measurements and a flowfield calculation give confidence that the PLIIF technique can be applied to more complex compressible flowfields with a reasonable level of accuracy. The technique has

been applied recently to a complete flowfield mapping experiment on a model combustor with an unswept ramp fuel injector.[15] The automated and improved technique reported herein was used to collect 35 planes of data in this complex three-dimensional flowfield.

V. Conclusions

The new Spectra-Physics 2080 laser used in this work has a wider gain profile than previous argon lasers, allowing access to additional iodine transitions at 514.5 nm. This permits a narrowband two-line planar temperature measurement technique to be used with the high-power argon laser and allows all flowfield parameters to be measured during a single tunnel run.

Use of the two-line planar temperature measurement technique has some important advantages relative to the broadband planar technique used previously. It removes systematic errors, such as local variations in the iodine seeding fraction. It is not restricted to pressures above 20 kPa, as required by the high-pressure limit in the broadband temperature method. Also, it does not require a point of known temperature for calibration purposes since it measures temperature absolutely.

Planar temperature and pressure measurements in the Mach 2 flow over a rearward-facing step are compared with a CFD calculation of the flowfield and to previous LIIF measurements. Deviation of near-wall temperature measurements from the calculation has decreased from about 21% with the previous planar method to less then 4% with the present technique. The improved measurement of temperature improves the accuracy of the pressure measurement because of the coupling of these thermodynamic variables. The velocity measurement accuracy also improved because the collisional impact shift is more accurately calculated with more accurate pressure and temperature measurements. Accuracies, for the range of conditions seen in the step flowfield studied, are estimated to be 5–8% for temperature, 4–12% for pressure, 10–20 m/s for velocity, and 2–3% for injectant mole fraction.

All aspects of data collection and control of the experiment are automated. The need to automate the measurement technique fully is apparent when the number of images files required for full flowfield mapping is considered. Difficulties in storing the large amounts of image data acquired and inconveniences from the long data reduction times have been alleviated by integrating a high-performance workstation into the experiment and by modifying the data reduction procedures. Data reduction times have been reduced by a factor of more than 50 compared with the previous technique.

Acknowledgments

This work has been supported by the NASA Langley Research Center under Grant NAG-1-795 and NASA Graduate Student Researchers Program Grant NGT-50897. The continued interest and support of G. Burton Northam, the Grant technical monitor, is gratefully acknowledged. The authors also wish to thank Dean R. Eklund for the SPARK CFD simulation and Kenneth G. Victor for his contributions to the completion of this work.

References

[1]McKenzie, R. L., "Progress in Laser-Spectroscopic Techniques for Aerodynamic Measurements—An Overview," AIAA Paper 91-0059, Jan. 1991.

[2]Rapagnani, N. L., and Davis, S. J., "Laser-Induced Iodine Fluorescence Measurements in a Chemical Laser Flowfield," *AIAA Journal*, Vol. 17, No. 12, 1979, pp. 1402–1404.

[3]Fletcher, D. G., and McDaniel, J. C., "Quantitative Characterization of a Nonreacting Supersonic Combustor Using Laser-Induced Iodine Fluorescence," AIAA Paper 89-2565, July 1989.

[4]Fletcher, D. G., "Spatially-Resolved, Nonintrusive Measurements in a Nonreacting Scramjet Combustor Using Laser-Induced Iodine Fluorescence," Ph.D. Dissertation, Dept. of Mechanical and Aerospace Engineering, Univ. of Virginia, Charlottesville, VA, Jan. 1989.

[5]Hartfield, R. J., Jr., Hollo, S. D., and McDaniel, J. C., "Planar Measurement Technique for Compressible Flows Using Laser-Induced Iodine Fluorescence," *AIAA Journal*, Vol. 31, No. 3, 1993, pp. 483–490.

[6]Hartfield, R. J., "Planar Measurement of Flow Field Parameters in Nonreacting Supersonic Flows with Laser-Induced Iodine Fluorescence," Ph.D. Dissertation, Dept. of Mechanical and Aerospace Engineering, Univ. of Virginia, Charlottesville, VA, May 1991.

[7]Fletcher, D. G., and McDaniel, J. C., "Temperature Measurement in a Compressible Flowfield Using Laser-Induced Iodine Fluorescence," *Optics Letters*, Vol. 12, No. 1, 1987, pp. 16–18.

[8]Ni-Imi, T., Fujimoto, T., and Shimizu, N., "Method for Planar Measurement of Temperature in Compressible Flow Using Two-Line Laser-Induced Iodine Fluorescence," *Optics Letters*, Vol. 15, No. 16, 1990, pp. 918–920.

[9]Hartfield, R. J., Jr., Hollo, S. D., and McDaniel, J. C., "Planar Temperature Measurement in Compressible Flows Using Laser-Induced Iodine Fluorescence," *Optics Letters*, Vol. 16, No. 2, 1991, pp. 106–108.

[10]Hartfield, R. J., Jr., Abbitt, J. D., III, and McDaniel, J. C., "Injectant Mole-Fraction Imaging in Compressible Mixing Flows Using Planar Laser-Induced Iodine Fluorescence," *Optics Letters*, Vol. 14, No. 16, 1989, pp. 850–852.

[11]Paul, P. H., Lee, M. P., and Hanson, R. K., "Molecular Velocity Imaging of Supersonic Flows Using Pulsed Planar Laser-Induced Fluorescence," *Optics Letters*, Vol. 14, No. 9, 1989, pp. 417–419.

[12]McDaniel, J. C., Hiller, B., and Hanson, R. K., "Simultaneous Multiple-Point Velocity Measurement Using Laser-Induced Iodine Fluorescence," *Optics Letters*, Vol. 8, No. 1, 1983, pp. 51–53.

[13]Hiller, B., and Hanson, R. K., "Simultaneous Planar Measurements of Velocity and Pressure Fields in Gas Flows Using Laser-Induced Fluorescence," *Applied Optics*, Vol. 27, No. 1, 1988, pp. 33–48.

[14]Hollo, S. H., Hartfield, R. J., and McDaniel, J. C., "Planar Velocity Measurement in Symmetric Flow Fields with Laser-Induced Iodine Fluorescence," *Optics Letters*, Vol. 19, No. 3, 1994, pp. 216–218.

[15]Donohue, J. M., and McDaniel, J. C., Jr., "Complete Three-Dimensional Multiparameter Mapping of a Supersonic Ramp Fuel Injector Flowfield," *AIAA Journal*, Vol. 34, No. 3, 1996, pp. 455–462; see also AIAA Paper 95-0519, Jan. 1995.

[16]McDaniel, J. C., "Investigation of Laser-Induced Fluorescence for Measurement of Density in Compressible Flows," Ph.D. Dissertation, Dept. of Aeronautics and Astronautics, Stanford Univ., Stanford, CA, Dec. 1981.

[17]Churassy, S., Grenet, G., Gaillard, M. L., and Bacis, R., "Hyperfine Structure in the B $\leftrightarrow$ X Transition of the Iodine Molecule Near the Head of the 12-0 Band, by Laser Spectroscopy of a Pure Iodine Supersonic Jet," *Optics Communications*, Vol. 30, No. 1, July 1979.

[18]Tellinghausen, J., "Intensity Factors for the I_2 B-X Band System," *Journal of Quantum Spectroscopy and Radiative Transfer*, Vol. 19, 1978, pp. 149–161.

[19]Gerstenkorn, S., and Luc, P., *Atlas du Spectre D'Absorption de la Molecule D'Iode*, Centre National de la Recherche Scientifique, Paris, 1978.

[20]McDaniel, J. C., "Laser Methods for Nonintrusive Measurement of Supersonic Hydrogen-Air Combustion Flowfields," Conf. Proceedings, ICALEO 1988, Laser Inst. of America, Vol. 67, 1988, pp. 209–218.

[21]Hollo, S. D., McDaniel, J. C., and Hartfield, R. J., Jr., "Characterization of Supersonic Mixing in a Nonreacting Mach 2 Combustor," AIAA Paper 92-0093, Jan. 1992.

[22]McDaniel, J. C., Fletcher, D., Hartfield, R., and Hollo, S., "Staged Transverse Injection Into Mach 2 Flow Behind a Rearward-Facing Step: A 3-D Compressible Test Case for Hypersonic Combustor Code Validation," AIAA Paper 91-5071, Dec. 1991.

[23]Drummond, J. P., "A Two Dimensional Numerical Simulation of a Supersonic, Chemically Reacting Mixing Layer," NASA TM-4055, Dec. 1988.

[24]Donohue, J. M., "Experimental and Numerical Study of Ramp Injectors for Supersonic Fuel/Air Mixing," Ph.D. Dissertation, Dept. of Mechanical, Aerospace and Nuclear Engineering, Univ. of Virginia, Charlottesville, VA, Jan. 1995.